Simulating Shear Wave Propagation in Two-Dimensional Fractured Heterogeneous Media by Coupling Boundary Element and Finite Difference Methods

Tianrun Chen, Junlun Li and Nafi Toksöz

Department of Earth, Atmospheric and Planetary Sciences, Massachusetts Institute of Technology, Cambridge, Massachusetts 02139

Abstract

A hybrid method to model the shear wave (SH) scattering from 2D fractures embedded in a heterogeneous medium is developed by coupling Boundary Element Method (BEM) and Finite Different Method (FDM) in the frequency domain. FDM is used to propagate an SH wave from a source through heterogeneities to localized homogeneous domains where fractures are embedded within artificial boundaries. According to Huygens' Principle, the boundary points can be regarded as "secondary" point sources and their values are determined by FDM. Given the incident fields from these point sources, BEM is applied to model scatterings from fractures and propagate them back to the artificial boundaries. FDM then takes the boundaries as secondary sources and continues propagating the scattered field into the heterogeneous medium. The hybrid method utilizes both the advantage of BEM and FDM. A numerical iterative scheme is also presented to account for the multiple scattering between different sets of fractures. The results calculated from this hybrid method with pure BEM method are first compared to show the accuracy of the hybrid approach and the iterative scheme. This method is then applied to calculate the wave scattered from fractures embedded in complex media.

PACS numbers:

I. INTRODUCTION

Precise modeling and understanding of seismic wave scattering from subsurface fractures in a heterogeneous medium is essential for imaging the fractures from seismic survey data. This forward modeling problem has been extensively discussed in the literature using different physical models of fractures,[1–3] combined with analytical[4,5] and numerical techniques, including Finite Difference Method (FDM),[6–12] Finite Element Method (FEM)[13] and Boundary Element Method (BEM).[14–16]

Liu et al.[4] applied representation theorems to calculate analytically the scattered waves from fractures based on Kirchhoff (high frequency) approximation. Sánchez-Sesma[5] applied an analytical approach to calculate scattering and diffraction from a crack with traction-free surface condition. Coates and Schoenberg[6] and Krüger et al.[7] used an effective medium theory and FDM to calculate seismic wave propagation through the fractures. Groenenboom[8] and Vlastos et al.[9] also used this effective medium theory to model wave scattering by hydraulic fractures and randomly distributed horizontal fractures, respectively. When dealing with fractures of complex geometries, the effective medium method may have accuracy issues due to the limitation of grid meshing in the traditional FDM. Instead of calculating the effective elastic constant of each mesh grid, Slawinski and Krebes[10], Zhang[11] and Zhang and Gao[12] directly impose the boundary conditions on auxiliary grid points surrounding the fractures. The complexity and computational cost of this method could be very demanding when non-planar fractures need to be considered, or when the distances between fractures are smaller than the seismic wavelength, as dense meshing is required. Nakagawa et al.[13] applied FEM to calculate 3D elastic wave scattering from parallel fractures in a single horizontal layer. Pointer[14], Iturrarán-Viveros et al.[15] and Iturrarán-Viveros et al.[16] applied an indirect boundary element method to calculate the scattered field from fractures and cracks. Chen et al.[17] applied BEM to model the scattering of SH waves from 2D fractures.

Compared to the analytical, FD, and FE methods, BEM is potentially more flexible and accurate in implementing complicated fracture boundary geometries and conditions.

Also BEM is more computationally efficient since it needs to compute one less space dimension compared to FDM or FEM. However, BEM requires an analytical expression of Green's functions of the medium; this is only available for few ideal scenarios such as homogeneous free space or half space. Meanwhile, the computational complexity and cost could dramatically increase for BEM to calculate scattering from fractures in a layered medium. These requirements and limitations restrict the applicable range of BEM in the real geophysical problems. Some authors have discussed hybrid methods by coupling BEM and other numerical methods. Bouchon and Coutant[18] developed a Boundary Element - Discrete Wavenumber Method. Since the Green's functions are evaluated by wavenumber summation, their method is suitable for propagating seismic waves in a layered homogeneous medium. Wuttke et al.[19] presented a coupling method between Boundary Integral Equation Method (BIEM) and Discrete Wavenumber method (DWN). DWN is used to propagate wave field in a horizontally layered medium, and BIEM is used to account for the effect of non-parallel layers and free surface on the wave propagation.

In this paper, we present a hybrid method to model the scattering from fractures in heterogeneous medium by coupling BEM and FDM. We use FDM to propagate an SH wave from the source through heterogeneities to localized homogeneous domains where fractures are embedded within artificial boundaries. According to Huygens' Principle, the boundary points can be regarded as "secondary" point sources and their values are determined by FDM. Given the incident fields from these point sources, we apply BEM to model the scattering from fractures and propagate them back to the artificial boundaries. FDM then takes the boundaries as secondary sources and continues propagating the scattered field into the heterogeneous medium. We developed an iterative scheme to account for the multiple scatterings between different sets of fractures, including the multiple interactions between fractures and surrounding medium heterogeneities. We also discuss the convergence conditions for the iterative scheme.

There are several advantages in our hybrid method. First, it overcomes the constraint of the simple homogeneous or layered medium in BEM while maintaining the flexibility of

BEM in handling boundary conditions and geometries of fractures. Second, it enables us to calculate scattering from fractures embedded in a complex medium without compromising the accuracy. Third, our approach can calculate the scattered field for different fracture distributions, source and receiver configurations, as well as source wavelets, efficiently. When using Monte-Carlo simulations to characterize the statistical properties of scattering from fractures, the efficiency issue becomes critical.

II. BEM AND FDM IN THE FREQUENCY DOMAIN

In this section, we briefly introduce BEM[17] to calculate SH wave scattering from fractures in a homogeneous free space, and FDM[20] to calculate the SH wave propagation in a heterogeneous medium.

A. BEM Modeling of Scattering from Fractures

The scattered displacement[21] from a fracture in the free space is

$$u_i^{\mathrm{sca}}(\boldsymbol{x}) = \int_s [u_k(\boldsymbol{\xi})] C_{kjqp}(\boldsymbol{\xi}) \frac{\partial G_i^p(\boldsymbol{x}, \boldsymbol{\xi})}{\partial \xi_q} \boldsymbol{n}_j(\boldsymbol{\xi}) \mathrm{d}\boldsymbol{\xi} \tag{1}$$

where $\boldsymbol{\xi}$ is a point on the 2D fracture surface s, as shown in Fig. 1; $C_{kjqp}(\boldsymbol{\xi})$ is the elastic tensor; $G_i^p(\boldsymbol{x}, \boldsymbol{\xi})$ is the i^{th} displacement component of the Green's function at point $\boldsymbol{x}$ due to a unit force in the p^{th} direction at point $\boldsymbol{\xi}$ on the fracture surface; $\boldsymbol{n}_j$ is the j^{th} component of the normal vector $\boldsymbol{n}$ at the fracture surface S; $[u_k(\boldsymbol{\xi})]$ is the k^{th} component of the displacement discontinuity

$$[u_k(\boldsymbol{\xi})] = u_k^+(\boldsymbol{\xi}) - u_k^-(\boldsymbol{\xi}), \tag{2}$$

where $u_k^+(\boldsymbol{\xi})$ and $u_k^-(\boldsymbol{\xi})$ is the total displacement on the upper and lower surface of fracture, respectively. The total displacement field $u_k(\boldsymbol{\xi})$ is the sum of the incident $u_k^i(\boldsymbol{x})$ and scattered displacement. In this paper, the displacement discontinuity is determined from the linear slip condition[1], which assumes that the displacement discontinuity is linearly proportional

to the traction on the fracture surface, and the traction is continuous across the fracture. For the SH wave, we have

$$\begin{aligned}[u_2(\boldsymbol{\xi})] &= Z_t(\boldsymbol{\xi})\big(\sigma_{21}(\boldsymbol{\xi})n_1(\boldsymbol{\xi}) + \sigma_{23}(\boldsymbol{\xi})n_3(\boldsymbol{\xi})\big) \\ &= Z_t(\boldsymbol{\xi})\big(\mu\frac{\partial u_2(\boldsymbol{\xi})}{\partial \xi_1}n_1(\boldsymbol{\xi}) + \mu\frac{\partial u_2(\boldsymbol{\xi})}{\partial \xi_3}n_3(\boldsymbol{\xi})\big). \end{aligned} \tag{3}$$

Inserting Equation 3 into Equation 1, we can express the scattered field as

$$u_2^{\mathrm{sca}}(\boldsymbol{x}) = \int_s Z_t(\boldsymbol{\xi})\mu^2\big(\frac{\partial u_2(\boldsymbol{\xi})}{\partial \xi_1}n_1(\boldsymbol{\xi}) + \frac{\partial u_2(\boldsymbol{\xi})}{\partial \xi_3}n_3(\boldsymbol{\xi})\big)\big(\frac{\partial G(\boldsymbol{x},\boldsymbol{\xi})}{\partial \xi_1}\boldsymbol{n}_1(\boldsymbol{\xi}) + \frac{\partial G(\boldsymbol{x},\boldsymbol{\xi})}{\partial \xi_3}\boldsymbol{n}_3(\boldsymbol{\xi})\big)\mathrm{d}.\boldsymbol{\xi} \tag{4}$$

The displacement at any $\boldsymbol{x}$ is the sum of the incident and scattered displacement

$$u_2(\boldsymbol{x}) = u_2^i(\boldsymbol{x}) + u_2^{\mathrm{sca}}(\boldsymbol{x}). \tag{5}$$

For a point on the fracture surface $\boldsymbol{x}(x_1, x_3) \in s$, it should satisfy Equation 5

$$u_2(\boldsymbol{x}) = u_2^i(\boldsymbol{x}) + \fint_s Z_t(\boldsymbol{\xi})\mu^2\big(\frac{\partial u_2(\boldsymbol{\xi})}{\partial \xi_1}n_1(\boldsymbol{\xi}) + \frac{\partial u_2(\boldsymbol{\xi})}{\partial \xi_3}n_3(\boldsymbol{\xi})\big)\big(\frac{\partial G(\boldsymbol{x},\boldsymbol{\xi})}{\partial \xi_1}\boldsymbol{n}_1(\boldsymbol{\xi}) + \frac{\partial G(\boldsymbol{x},\boldsymbol{\xi})}{\partial \xi_3}\boldsymbol{n}_3(\boldsymbol{\xi})\big)\mathrm{d}\boldsymbol{\xi}, \tag{6}$$

where $\fint_s$ donates the hyper-singular integral equation or a Cauchy's principal value. We take derivatives of Equation 6 over x_1 and x_3, respectively

$$\begin{aligned}\frac{\partial u_2(\boldsymbol{x})}{\partial x_1} &= \frac{\partial u_2^i(\boldsymbol{x})}{\partial x_1} \\ &+ \fint_s Z_t(\boldsymbol{\xi})\mu^2\big(\frac{\partial u_2(\boldsymbol{\xi})}{\partial \xi_1}n_1(\boldsymbol{\xi}) + \frac{\partial u_2(\boldsymbol{\xi})}{\partial \xi_3}n_3(\boldsymbol{\xi})\big)\big(\frac{\partial^2 G(\boldsymbol{x},\boldsymbol{\xi})}{\partial \xi_1 \partial x_1}\boldsymbol{n}_1(\boldsymbol{\xi}) + \frac{\partial^2 G(\boldsymbol{x},\boldsymbol{\xi})}{\partial \xi_3 \partial x_1}\boldsymbol{n}_3(\boldsymbol{\xi})\big)\mathrm{d}\boldsymbol{\xi}, \end{aligned} \tag{7}$$

and

$$\begin{aligned}\frac{\partial u_2(\boldsymbol{x})}{\partial x_3} &= \frac{\partial u_2^i(\boldsymbol{x})}{\partial x_3} \\ &+ \fint_s Z_t(\boldsymbol{\xi})\mu^2\big(\frac{\partial u_2(\boldsymbol{\xi})}{\partial \xi_1}n_1(\boldsymbol{\xi}) + \frac{\partial u_2(\boldsymbol{\xi})}{\partial \xi_3}n_3(\boldsymbol{\xi})\big)\big(\frac{\partial^2 G(\boldsymbol{x},\boldsymbol{\xi})}{\partial \xi_1 \partial x_3}\boldsymbol{n}_1(\boldsymbol{\xi}) + \frac{\partial^2 G(\boldsymbol{x},\boldsymbol{\xi})}{\partial \xi_3 \partial x_3}\boldsymbol{n}_3(\boldsymbol{\xi})\big)\mathrm{d}\boldsymbol{\xi}, \end{aligned} \tag{8}$$

by applying a theorem proved by[22]. We now turn the displacement boundary integral equation (1) into two traction-related boundary integral equations (7 and 8). Solving these

two equations provides values of the displacement derivative $\frac{\partial u_2(\boldsymbol{x})}{\partial x_1}$ and $\frac{\partial u_2(\boldsymbol{x})}{\partial x_3}$ across the fracture. By inserting these two derivatives into Equation 4, the displacement field scattered from the 2D fracture can be finally calculated. Also, the derivative of the scattered field is

$$\frac{\partial u_2^{\mathrm{sca}}(\boldsymbol{x})}{\partial \boldsymbol{x}} = \int_s Z_t(\boldsymbol{\xi})\mu^2\big(\frac{\partial u_2(\boldsymbol{\xi})}{\partial \xi_1}n_1(\boldsymbol{\xi}) + \frac{\partial u_2(\boldsymbol{\xi})}{\partial \xi_3}n_3(\boldsymbol{\xi})\big)\big(\frac{\partial^2 G(\boldsymbol{x},\boldsymbol{\xi})}{\partial \xi_1 \partial \boldsymbol{x}}\boldsymbol{n}_1(\boldsymbol{\xi}) + \frac{\partial^2 G(\boldsymbol{x},\boldsymbol{\xi})}{\partial \xi_3 \partial \boldsymbol{x}}\boldsymbol{n}_3(\boldsymbol{\xi})\big)\mathrm{d}\boldsymbol{\xi}, \tag{9}$$

which is needed in the coupling of BEM with FDM.

B. FDM to Model Wave Propagation in an Heterogeneous Medium

In the frequency domain, the SH wave equation is

$$\frac{\partial}{\partial x}\big[\frac{1}{\rho(x,z)}\frac{\partial}{\partial x}u(x,z,\omega)\big] + \frac{\partial}{\partial z}\big[\frac{1}{\rho(x,z)}\frac{\partial}{\partial z}u(x,z,\omega)\big] + \frac{\omega^2}{\mu(x,y)}u(x,z,\omega) = s(x,z,\omega), \tag{10}$$

where $\rho(x,z)$ is the density, $u(x,z,\omega)$ is the displacement, ω is the angular frequency, $\mu(x,z)$ is the modulus of rigidity, and $s(x,z,\omega)$ is the source term. We discretize Equation 10 with a low-dispersion fourth-order finite difference scheme in space by following Equation A3 in Ref.20

$$\begin{aligned}
\frac{-\omega^2}{K_{i,j}}u_{i,j} = \frac{1}{\Delta^2}\Big\{\frac{9}{8}\Big[\frac{1}{\rho_{i+1/2,j}}\big(\frac{9}{8}(u_{i+1,j}-u_{i,j}-\frac{1}{24}(u_{i+2,j}-u_{i-1,j})\big) \\
-\frac{1}{\rho_{i-1/2,j}}\big(\frac{9}{8}(u_{i,j}-u_{i-1,j}-\frac{1}{24}(u_{i+1,j}-u_{i-2,j})\big)\Big] \\
-\frac{1}{24}\Big[\frac{1}{\rho_{i+3/2,j}}\big(\frac{9}{8}(u_{i+2,j}-u_{i+1,j})-\frac{1}{24}(u_{i+3,j}-u_{i,j}) \\
-\frac{1}{\rho_{i-3/2,j}}\big(\frac{9}{8}(u_{i-1,j}-u_{i-2,j})-\frac{1}{24}(u_{i,j}-u_{i-3,j})\Big]\Big\} \\
+\frac{1}{\Delta^2}\Big\{\frac{9}{8}\Big[\frac{1}{\rho_{i,j+1/2}}\big(\frac{9}{8}(u_{i,j+1}-u_{i,j}-\frac{1}{24}(u_{i,j+2}-u_{i,j-1})\big) \\
-\frac{1}{\rho_{i,j-1/2}}\big(\frac{9}{8}(u_{i,j}-u_{i,j-1}-\frac{1}{24}(u_{i,j+1}-u_{i,j-2})\big)\Big] \\
-\frac{1}{24}\Big[\frac{1}{\rho_{i,j+3/2}}\big(\frac{9}{8}(u_{i,j+2}-u_{i,j+1})-\frac{1}{24}(u_{i,j+3}-u_{i,j}) \\
-\frac{1}{\rho_{i,j-3/2}}\big(\frac{9}{8}(u_{i,j-1}-u_{i,j-2})-\frac{1}{24}(u_{i,j}-u_{i,j-3})\Big]\Big\} + S_{i,j}.
\end{aligned} \tag{11}$$

We use a regular finite-difference scheme instead of the mixed-grid scheme[20]. This is because point source excitation in the mixed-grid scheme would result in numerical noises and obscuring the weak scattered field. In general, Equation 11 can be written as

$$Au = S, \tag{12}$$

where A is the impedance matrix constructed by the FD operators shown in Equation 11 and S is the source vector. To solve Equation 12, we can use the LU factorization[23] to decompose matrix A. We also implement the Perfectly Matched Layers (PMLs) in the surrounding areas to absorb outgoing waves.

III. HYBRID METHOD

In this section, we first introduce the approach to coupling BEM with FDM for calculating the primary scattering from an individual set of fractures without considering the second or higher order interactions either between different sets of fractures or between fractures and heterogeneities. Then, we will discuss an iterative method to include the higher order scatterings.

A. Coupling between BEM and FDM

The basic idea of the hybrid method is to use a boundary integral equation and local Green's functions to represent a global Green's function, which can not be expressed analytically due to the presence of heterogeneities, as shown in Fig. 2. The local domain hosting fractures is surrounded by an artificial closed boundary Γ. Although embedded in a heterogeneous medium, this small local domain can be reasonably assumed to be homogeneous. According to representation theorems, we can express the global displacement Green's function in terms of the combination of the local Green's functions and the normal derivatives of local Green's functions along boundary Γ

$$G(\boldsymbol{x}, \boldsymbol{x}_0) = \oint_\Gamma \big[\frac{\partial u(\boldsymbol{\xi}, \boldsymbol{x}_0)}{\partial \mathbf{n}} G(\boldsymbol{x}, \boldsymbol{\xi}) - u(\boldsymbol{\xi}, \boldsymbol{x}_0) \frac{\partial G(\boldsymbol{x}, \boldsymbol{\xi})}{\partial \mathbf{n}}\big] \mathrm{d}\boldsymbol{\xi}, \tag{13}$$

where $\boldsymbol{x}_0$ and $\boldsymbol{x}$ are the source and receiver position, respectively; $\boldsymbol{\xi}$ is a point at Γ. The displacement Green's function for SH wave in a 2D homogeneous medium is

$$G(\boldsymbol{x},\boldsymbol{\xi}) = \frac{i}{4\pi\mu} H_0(k|\boldsymbol{x}-\boldsymbol{\xi}|). \tag{14}$$

where H_0 is zero order Hankel function. Note that $G(\boldsymbol{x},\boldsymbol{\xi})$ and $\frac{\partial G(\boldsymbol{x},\boldsymbol{\xi})}{\partial \mathbf{n}}$ in Equation 13 represent a monopole and dipole source, respectively, whose amplitude $\frac{\partial u(\boldsymbol{\xi},\boldsymbol{x}_0)}{\partial \mathbf{n}}$ and $-u(\boldsymbol{\xi},\boldsymbol{x}_0)$ are determined by FDM.

To couple FDM and BEM, we first need to discretize the boundary Γ to Γ_{FDM} composed of regular finite difference grids, as shown in Fig. 3. The reason for placing two boundaries Γ_{FDM} and Γ_{BEM} in the coupling scheme will be elaborated in Section III.B. Using the grid points as secondary sources, we can construct the incident field for fractures surrounded by Γ_{FDM} and discretize Equation 13 to

$$G(\boldsymbol{x},\boldsymbol{x}_0) \approx G^{\mathrm{upper}} + G^{\mathrm{down}} + G^{\mathrm{left}} + G^{\mathrm{right}} \tag{15}$$

where

$$\begin{aligned}
G^{\mathrm{upper}} &= \sum_{i=2}^{M-1} \big[-\frac{\partial u(\boldsymbol{\xi}_i,\boldsymbol{x}_0)}{\partial y} G(\boldsymbol{x},\boldsymbol{\xi}_i) + u(\boldsymbol{\xi}_i,\boldsymbol{x}_0)\frac{\partial G(\boldsymbol{x},\boldsymbol{\xi}_i)}{\partial y}\big]\Delta \\
&\quad + \frac{1}{2}\sum_{i=1,i=M} \big[-\frac{\partial u(\boldsymbol{\xi}_i,\boldsymbol{x}_0)}{\partial y} G(\boldsymbol{x},\boldsymbol{\xi}_i) + u(\boldsymbol{\xi}_i,\boldsymbol{x}_0)\frac{\partial G(\boldsymbol{x},\boldsymbol{\xi}_i)}{\partial y}\big],\Delta \\
G^{\mathrm{lower}} &= \sum_{j=2}^{M-1} \big[\frac{\partial u(\boldsymbol{\xi}_j,\boldsymbol{x}_0)}{\partial y} G(\boldsymbol{x},\boldsymbol{\xi}_j) - u(\boldsymbol{\xi}_j,\boldsymbol{x}_0)\frac{\partial G(\boldsymbol{x},\boldsymbol{\xi}_j)}{\partial y}\big]\Delta \\
&\quad + \frac{1}{2}\sum_{j=1,j=M} \big[\frac{\partial u(\boldsymbol{\xi}_j,\boldsymbol{x}_0)}{\partial y} G(\boldsymbol{x},\boldsymbol{\xi}_j) - u(\boldsymbol{\xi}_j,\boldsymbol{x}_0)\frac{\partial G(\boldsymbol{x},\boldsymbol{\xi}_j)}{\partial y}\big],\Delta \\
G^{\mathrm{left}} &= \sum_{l=2}^{N-1} \big[-\frac{\partial u(\boldsymbol{\xi}_l,\boldsymbol{x}_0)}{\partial x} G(\boldsymbol{x},\boldsymbol{\xi}_l) + u(\boldsymbol{\xi}_l,\boldsymbol{x}_0)\frac{\partial G(\boldsymbol{x},\boldsymbol{\xi}_l)}{\partial x}\big]\Delta \\
&\quad + \frac{1}{2}\sum_{l=1,l=N} \big[-\frac{\partial u(\boldsymbol{\xi}_l,\boldsymbol{x}_0)}{\partial x} G(\boldsymbol{x},\boldsymbol{\xi}_l) + u(\boldsymbol{\xi}_l,\boldsymbol{x}_0)\frac{\partial G(\boldsymbol{x},\boldsymbol{\xi}_l)}{\partial x}\big],\Delta \\
G^{\mathrm{right}} &= \sum_{k=2}^{N-1} \big[\frac{\partial u(\boldsymbol{\xi}_k,\boldsymbol{x}_0)}{\partial x} G(\boldsymbol{x},\boldsymbol{\xi}_k) - u(\boldsymbol{\xi}_k,\boldsymbol{x}_0)\frac{\partial G(\boldsymbol{x},\boldsymbol{\xi}_k)}{\partial x}\big]\Delta \\
&\quad + \frac{1}{2}\sum_{k=1,k=N} \big[\frac{\partial u(\boldsymbol{\xi}_k,\boldsymbol{x}_0)}{\partial x} G(\boldsymbol{x},\boldsymbol{\xi}_k) - u(\boldsymbol{\xi}_k,\boldsymbol{x}_0)\frac{\partial G(\boldsymbol{x},\boldsymbol{\xi}_k)}{\partial x}\big]\Delta,
\end{aligned} \tag{16}$$

where Δ is the FD discretization length, M and N are the total grid points along horizontal and vertical directions. Since the corner points only span half-grid length compared to the rest of the points, a weight 1/2 in Equation 16 is used to account for this difference. The amplitudes of *dipole sources*, $u(\boldsymbol{\xi}_i, \boldsymbol{x}_0)$, $-u(\boldsymbol{\xi}_j, \boldsymbol{x}_0)$, $u(\boldsymbol{\xi}_k, \boldsymbol{x}_0)$ and -$u(\boldsymbol{\xi}_l, \boldsymbol{x}_0)$, can be obtained directly from FDM. The amplitudes of the *monopole sources*, $-\frac{\partial u(\boldsymbol{\xi}_i, \boldsymbol{x}_0)}{\partial y}$, $\frac{\partial u(\boldsymbol{\xi}_j, \boldsymbol{x}_0)}{\partial y}$, $-\frac{\partial u(\boldsymbol{\xi}_k, \boldsymbol{x}_0)}{\partial x}$ and $\frac{\partial u(\boldsymbol{\xi}_l, \boldsymbol{x}_0)}{\partial x}$, however, need to be evaluated via a fourth-order finite difference approximation, for being consistent with the global fourth-order accuracy of FDM scheme. For instance, the displacement gradient at point ξ_n (Fig. 3) is

$$\frac{\partial u(\boldsymbol{\xi}_n, \boldsymbol{x}_0)}{\partial x} = \frac{-\frac{2}{3}u(\boldsymbol{\xi}_{n-1}, \boldsymbol{x}_0) + \frac{2}{3}u(\boldsymbol{\xi}_{n+1}, \boldsymbol{x}_0) + \frac{1}{12}u(\boldsymbol{\xi}_{n-2}, \boldsymbol{x}_0) - \frac{1}{12}u(\boldsymbol{\xi}_{n+2}, \boldsymbol{x}_0)}{\Delta}, \tag{17}$$

which requires the displacement values at four different grids, with two inside and two outside boundary Γ_{FDM}.

After the amplitudes of surrounding monopole and dipole sources are determined, we can adopt BEM to calculate the displacement discontinuities across the upper and lower surfaces of the fractures subjected to the incidence from the surrounding sources. Given the displacement discontinuities, the scattered field u_2^{sca} and the normal derivative of the scattered field $\frac{\partial u_2^{\mathrm{sca}}}{\partial \mathbf{n}}$ at another boundary Γ_{BEM} are calculated analytically via Equations 4 and 9.

Finally, we rely on FDM to propagate the scattered field at Γ_{BEM} outward to any outside location $\boldsymbol{x}$ via

$$u^{\mathrm{sca}}(\boldsymbol{x}) = \oint_{\Gamma_{\mathrm{BEM}}} \Big[\frac{\partial u_2^{\mathrm{sca}}(\boldsymbol{\xi}')}{\partial \mathbf{n}} G(\boldsymbol{x}, \boldsymbol{\xi}') - u_2^{\mathrm{sca}}(\boldsymbol{\xi}') \frac{\partial G(\boldsymbol{x}, \boldsymbol{\xi}')}{\partial \mathbf{n}}\Big] \mathrm{d}\boldsymbol{\xi}', \tag{18}$$

where $\boldsymbol{\xi}' \in \Gamma_{\mathrm{BEM}}$. The Green's function $G(\boldsymbol{x}, \boldsymbol{\xi}')$ (monopole source) is directly implemented by FDM, while the dipole source at ξ_n' needs to be implemented by

$$u_2^{\mathrm{sca}}(\boldsymbol{\xi}_n') \frac{\partial G(\boldsymbol{x}_n, \boldsymbol{\xi}_n')}{\partial \boldsymbol{n}} = u_2^{\mathrm{sca}}(\boldsymbol{\xi}_n') \frac{\frac{2}{3}G(\boldsymbol{x}, \boldsymbol{\xi}_{n-1}') - \frac{2}{3}G(\boldsymbol{x}, \boldsymbol{\xi}_{n+1}') + \frac{1}{12}G(\boldsymbol{x}, \boldsymbol{\xi}_{n-2}') - \frac{1}{12}G(\boldsymbol{x}, \boldsymbol{\xi}_{n+2}')}{\Delta}, \tag{19}$$

which requires implementation of four monopole sources at ξ_{n-2}', ξ_{n-1}', ξ_{n+1}' and ξ_{n+2}', as shown in Fig. 3. The numerical implementation of the monopole term in Equation 18

requires injecting the source excitation $\frac{\partial u_2^{\mathrm{sca}}(\boldsymbol{\xi}^{'})}{\partial \mathbf{n}}$ in the RHS of Equation 12 at the corresponding position $\boldsymbol{\xi}^{'}$; the dipole term requires injecting the source excitations $2u_2^{\mathrm{sca}}(\boldsymbol{\xi}^{'})/3\Delta$, $-2u_2^{\mathrm{sca}}(\boldsymbol{\xi}^{'})/3\Delta$, $u_2^{\mathrm{sca}}(\boldsymbol{\xi}^{'})/12\Delta$ and $-u_2^{\mathrm{sca}}(\boldsymbol{\xi}^{'})/12\Delta$ at four postions in the RHS of Equation 12.

The aforementioned BEM can be applied to calculate multiple interactions among fractures embedded within the same local domain.[17] When the separation between different fractures is larger than the wavelength, it is unrealistic to circumscribe all fractures into one big domain and assume the homogeneity of the whole domain. Therefore, we need an iterative method to include the multiple scatterings, as discussed in Section III.B.

B. Iterative Method for Multiple Scattering

In this section, we show how to apply an iterative method to calculate the multiple scattering between different sets of fractures or between fractures and heterogeneities. The idea of the iterative scheme is to calculate Born series to account for multiple scattering. In the Appendix, we briefly discuss the convergence conditions of the iterative scheme for the multiple scatterings.

To simplify the discussion, we assume that there are two sets of fractures A and B embedded in a heterogeneous medium. We first calculate the primary scattered field u_A^{sca} and u_B^{sca} from fracture set A and B individually, and then use FDM to propagate them outward simultaneously into the heterogeneous medium. After some interactions with heterogeneities, the primary scatterings propagate onto both fracture sets A and B, hence resulting in second scatterings. To calculate the second scattered field, we follow the same procedure described in Section. III.A. For fracture set A, the incident wave field along $\Gamma_{\mathrm{FDM}}^{A}$ is

$$u^{\mathrm{inc2}}(\boldsymbol{x}) = \oint_{\Gamma_{\mathrm{FDM}}^{A}} \Big[\frac{\partial u^{\mathrm{sca}}(\boldsymbol{\xi})}{\partial \mathbf{n}} G(\boldsymbol{x},\boldsymbol{\xi}) - u^{\mathrm{sca}}(\boldsymbol{\xi}) \frac{\partial G(\boldsymbol{x},\boldsymbol{\xi})}{\partial \mathbf{n}}\Big] \mathrm{d}\boldsymbol{\xi} \tag{20}$$

where $u^{\mathrm{sca}}(\boldsymbol{\xi})$ is calculated by

$$u^{\mathrm{sca}}(\boldsymbol{\xi}) = \oint_{\Gamma^A_{\mathrm{BEM}}} \big[\frac{\partial u^{\mathrm{sca}}_A(\boldsymbol{\xi}')}{\partial \mathbf{n}} G(\boldsymbol{\xi},\boldsymbol{\xi}') - u^{\mathrm{sca}}_A(\boldsymbol{\xi}')\frac{\partial G(\boldsymbol{\xi},\boldsymbol{\xi}')}{\partial \mathbf{n}}\big]\mathrm{d}\boldsymbol{\xi}' + \oint_{\Gamma^B_{\mathrm{BEM}}} \big[\frac{\partial u^{\mathrm{sca}}_B(\boldsymbol{\xi}')}{\partial \mathbf{n}} G(\boldsymbol{\xi},\boldsymbol{\xi}') - u^{\mathrm{sca}}_B(\boldsymbol{\xi}')\frac{\partial G(\boldsymbol{\xi},\boldsymbol{\xi}')}{\partial \mathbf{n}}\big]\mathrm{d}\boldsymbol{\xi}', \tag{21}$$

which originates from the primary scattered fields u^{sca}_A and u^{sca}_B, propagated numerically by FDM. The incident field on fractures set B is calculated with the same method. BEM is applied again to calculate the second scattering u^{sca2}_A and u^{sca2}_B from fracture A and B due to the new incident field u^{inc2}. Afterwards, FDM is used to propagate the second scattered fields u^{sca2}_A and u^{sca2}_B outward. We iterate the above steps to account for the multiple scatterings until the energy of the higher scattering is negligible. The iterative scheme (Equations 20 and 21) assures the causality such that a lower scattering is the source for the next higher scattering. The temporal sequence of the different orders of the scattered field is determined implicitly by the phases.

We use boundary Γ_{FDM} when propagating the wave field by FDM into a local domain, and use the boundary Γ_{BEM} to propagate the scattered field out of the local domain, as shown in Fig. 3. According to Huygens' principle, Γ_{BEM} is an outward-radiation boundary. As a result, Equation 18 can only provide the correct primary scattered field $u^{\mathrm{sca}}(\boldsymbol{x})$ at $\boldsymbol{x}$ *outside* the domain surrounded by Γ_{BEM}, but not for any point *within* Γ_{BEM}. This causes issues for the calculation of secondary scattering from fractures, e.g., the calculation of the displacement gradient $\frac{\partial u^{\mathrm{sca}}(\boldsymbol{\xi}_i)}{\partial x}$ for a grid point m at Γ_{FDM} requires displacement values $u^{\mathrm{sca}}(\boldsymbol{\xi}_{m-1})$, $u^{\mathrm{sca}}(\boldsymbol{\xi}_{m-2})$, $u^{\mathrm{sca}}(\boldsymbol{\xi}_{m+1})$ and $u^{\mathrm{sca}}(\boldsymbol{\xi}_{m+2})$ at four different grids according to Equation 17. If the separation between Γ_{FDM} and Γ_{BEM} is smaller than two grids, $u^{\mathrm{sca}}(\boldsymbol{\xi}_{m+1})$ and $u^{\mathrm{sca}}(\boldsymbol{\xi}_{m+2})$ could fall inside the domain surrounded by Γ_{BEM} and then their values are not calculated correctly. This leads to an incorrect computation of $\frac{\partial u^{\mathrm{sca}}(\boldsymbol{\xi}_m)}{\partial x}$. We can easily solve this issue by placing Γ_{FDM} two grids bigger than Γ_{BEM}. It should be noted that these two boundaries can be collocated if we only consider the primary scattering from the fractures.

C. Monte-Carlo Simulations

In order to perform Monte-Carlo simulations to characterize the statistical properties of scattering from fractures, we need to calculate the scattering from random fracture realizations. Given that the background medium remains unchanged and does not depend on the geometries and properties of fractures, we only need to perform the LU factorization, which takes a major part of the computational time, to the impedance matrix A *once* for each frequency

$$L(\omega) \cdot U(\omega) = P(\omega) \cdot A(\omega) \cdot Q(\omega), \tag{22}$$

where $L(\omega)$ and $U(\omega)$ are the lower and upper triangular matrices, respectively; $P(\omega)$ and $Q(\omega)$ are the row and column permutation matrices for numerical stability. To calculate the response of the medium to different source excitation $S(\omega)$, e.g., point sources or secondary sources from fracture scatterings, we only change the right-hand side of Equation 12 with the corresponding source term. Given L, U, P and Q, solving Equation 12 takes negligible computational time. Therefore, Monte-Carlo simulations can be implemented very efficiently.

IV. NUMERICAL EXAMPLES

In this section, we first provide two examples that compare the results from the hybrid method with the ones from the BEM in a homogeneous medium. Then, we show the simulations of the scattered waves from fractures embedded in a horizontally layered medium and a more complex Marmousi model.

For the first example, a horizontal fracture is embedded in a homogeneous medium with $V_s = 2500\ m/s$ and $\rho = 2200\ kg/m^3$, as shown in Fig. 4. The tangential compliance of the fracture is $10^{-9}\ m/Pa$. The fracture is 100 m in length. We denote the local domain with a white box surrounded by the artificial boundary Γ_{BEM}. The source has a unit amplitude. The frequency of the incident wave is 20 Hz, corresponding to a wavelength of 125 m.

The black dot represents the source location, and the white crosses represent the receiver locations. Fig. 4 shows the amplitude of the scattered field, which exhibits strong scattering patterns in the forward and backward directions. The tip scattering from the fracture is relatively weak due to the direction of the incident wave. Fig. 5 compares the amplitude and phase of the scattered field between the hybrid method and BEM. The maximum difference in both amplitude and phase is less than one percent.

In the second example, we have four inclined fractures embedded in the same background medium as in the previous example (Fig. 6). The incident field is also the same as in the first example. The total scattered field shows a strong interference pattern, particularly between the inner pair of fractures. The scattering in the forward direction is much stronger than in the backward direction. We use the iterative method to calculate the multiple scattering between different fractures (Fig. 7). Since the first iteration only includes the single scatterings from each fracture, there is some difference with the BEM solution. After five iterations, the result from the hybrid method converges to the result from BEM, with the difference smaller than one percent.

In most real cases, velocity heterogeneities exist and obscure the scattering signals from the fractures. In the next two examples, we show the scatterings from fractures embedded in a layered model and a modified Marmousi model. For the layered model as shown in Fig. 8, we placed 12 randomly distributed fractures, four of which cross each other within the same artificial boundaries. The densities for the three layers from top to bottom are 2000 kg/m^3, 2200 kg/m^3, 2500 kg/m^3, respectively. The compliance of each fracture is $5 \times 10^{-10} m/Pa$. Fig. 9 shows the incident waves (red) and the scattered waves (blue) at the receivers. The incident waves refer to the response of the background medium to the source excitation. We see clear direct arrivals and primary reflections from the layer interfaces, while weak multiple reflections among the interfaces are difficult to observe. The scattered waves (amplitudes amplified by ten times to show the details) arrive between the primary reflections from interfaces, as expected. The scatterings from the fractures consist of single scattering from tips of fractures, multiple scatterings among fractures, as well as multiple

interactions between fractures and layer interfaces. The scattered waves show a coherent pattern, e.g., similar waveforms are observed at different receivers with varying delay times.

We also placed 12 randomly distributed fractures in a modified Marmousi model (Fig. 10). The fractures have varying lengths and inclinations, but are with the same compliance ($5 \times 10^{-10} m/Pa$). In an ideal case, our hybrid scheme requires homogeneity within the boundary Γ_{FDM}. Practically, if the medium heterogeneity is weak within Γ_{FDM} and the medium is approximately homogeneous, our hybrid scheme can still be applicable. The incident waves show complex patterns due to the significant heterogeneities of the model, and the signals arrived after 1 s are relatively weak, as shown in Fig. 11 (a). In comparison, multiple scatterings from fractures reverberate between 0.6 s and 1.5 s. Though propagating through the complex model, coherent patterns can still be observed in the scattered waves. Figs. 11 (c) and (b) shows a typical incident waveform and a scattered waveform at a receiver ('diamond' in Fig. 10). The maximum amplitude of the scattered wave is about 2 percent of that of the incident wave.

The amplitudes of the multiple scatterings decay with the increasing scattering orders, and are negligible after the 5^{th} iteration (Fig. 12). Also, the arrival times of the scattered waves of different orders are monotonically delayed, since higher order scatterings take longer time to propagate among fractures before arriving at the receivers. We also found that the dominant energy spectrum shifts to higher frequency band with the increasing scattering order, as higher frequency contents are scattered more strongly by the fractures.

V. CONCLUSION

In this paper, we proposed a hybrid method in the frequency domain to model the SH wave scatterings from fractures embedded in a 2D heterogeneous medium by coupling BEM and FDM through two artificial coupling boundaries. We also presented an iterative scheme to account for the multiple scatterings between different sets of fractures including the multiple interactions between fractures and surrounding medium heterogeneities. We

showed the accuracy of our method by comparing the results with those from pure BEM. The hybrid method can be applied to calculate scattering from fractures with arbitrary geometries embedded in a complex heterogeneous medium. With the efficiency of our hybrid method, it can potentially be used to perform Monte-Carlo simulations to characterize the statistics of scattering signals from subsurface fracture networks.

APPENDIX A: CONVERGENCE CONDITIONS OF THE ITERATIVE SCHEME FOR THE MULTIPLE SCATTERINGS

In this section, we briefly discuss the convergence condition of the multiple scatterings between different fractures, i.e., the Born series.

We start with a simple scenario of two fractures A and B embedded in a free homogeneous space. We can express Equations 7 and 8 in terms of

$$\begin{bmatrix} A & A_b \\ B_a & B \end{bmatrix} \begin{bmatrix} U^a_{\text{sca}} \\ U^b_{\text{sca}} \end{bmatrix} = \begin{bmatrix} u^a_{\text{inc}} \\ u^b_{\text{inc}} \end{bmatrix} \tag{A1}$$

where A and B are the matrices that characterize the response of fracture A and B to an external field, such as the incident field or the scattered field; A_b is a propagator matrix (Green's function) that propagates the response from fracture B to fracture A and vice versa for B_a; $U_{\text{sca}} = [u]$ is displacement discontinuity on the surfaces of the fractures due to the exnternal field. Since A_b and B_a can only be calculated numerically for a heterogeneous medium, we can not solve Equation A1 directly and need the iteration scheme to account the multiple interactions.

The first order Born scattered fields are

$$\begin{aligned} U^a_{\text{sca}} &= A^{-1} u^a_{\text{inc}} \\ U^b_{\text{sca}} &= B^{-1} u^b_{\text{inc}} \end{aligned} \tag{A2}$$

where u^a_{inc} and u^b_{inc} are the incident field on fracture A and B, respectively. The second order Born scattered fields are

$$\begin{aligned} U^{ab}_{\text{sca}} &= (A^{-1} A_b) U^b_{\text{sca}} = (A^{-1} A_b) B^{-1} u^b_{\text{inc}} \\ U^{ba}_{\text{sca}} &= (B^{-1} B_a) U^a_{\text{sca}} = (B^{-1} B_a) A^{-1} u^a_{\text{inc}}, \end{aligned} \tag{A3}$$

where U^{ab}_{sca} originates from the scattering of fracture B (U^b_{sca}), propagated through the medium (A_b) and causing the response on fracture A (A^{-1}). Similarly, the third Born

scatterings are

$$U_{\text{sca}}^{aba} = (A^{-1}A_b)U_{\text{sca}}^{ba} = (A^{-1}A_b)(B^{-1}B_a)A^{-1}U_{\text{inc}}^{a}$$
$$U_{\text{sca}}^{bab} = (B^{-1}B_a)U_{\text{sca}}^{ab} = (B^{-1}B_a)(A^{-1}A_b)B^{-1}U_{\text{inc}}^{b} \tag{A4}$$

by adding iteration factors $A^{-1}A_b$ and $B^{-1}B_a$ to the second order Born scattering. The next order scattered field can also be calculated by adding the iteration factors to the scattered field of the previous order. To guarantee the convergence of the multiple scattering series, the spectral radii of the iteration factors (maximum absolute eigenvalue) needs to be smaller than 1[24]

$$\max|\lambda(A^{-1}A_b)| < 1$$
$$\max|\lambda(B^{-1}B_a)| < 1.$$

For a scenario of N fractures, we have

$$\begin{bmatrix} F_{11} & F_{12} & F_{13} & ... & F_{1n} \\ F_{21} & F_{22} & F_{23} & ... & F_{2n} \\ ... & ... & ... & ... & ... \\ ... & ... & ... & ... & ... \\ F_{n1} & F_{n2} & F_{n3} & ... & F_{nn} \end{bmatrix} \begin{bmatrix} U_{\text{sca}}^{1} \\ U_{\text{sca}}^{2} \\ U_{\text{sca}}^{3} \\ ... \\ U_{\text{sca}}^{n} \end{bmatrix} = \begin{bmatrix} u_{\text{inc}}^{1} \\ u_{\text{inc}}^{2} \\ u_{\text{inc}}^{3} \\ ... \\ u_{\text{inc}}^{n}. \end{bmatrix} \tag{A5}$$

where F_{ii} is the matrix that characterizes the response of fracture i to the external field and $F_{ij}(i \neq j)$ is the propagator that propagates the response from fracture j to fracture i.

The first Born scattering for the i^{th} fracture is

$$U_{\text{sca}}^{i1} = F_{ii}^{-1}U_{\text{inc}}^{i}. \tag{A6}$$

The second Born scattering for the i^{th} fracture is

$$U_{\text{sca}}^{i2} = \sum_{j=1,j\neq i}^{N} (F_{ii}^{-1}F_{ij})U_{\text{sca}}^{j1} = \sum_{j=1,j\neq i}^{N} (F_{ii}^{-1}F_{ij})F_{jj}^{-1}U_{\text{inc}}^{j} \tag{A7}$$

The third Born scattering for the i^{th} fracture is

$$U_{\text{sca}}^{i3} = \sum_{j=1,j\neq i}^{N} (F_{ii}^{-1}F_{ij})U_{\text{sca}}^{j2}. \tag{A8}$$

The higher order scattered fields can also be derived in the similar way.

To converge the multiple scatterings, the maximum absolute eigenvalue of the iteration factors summation needs to satisfy

$$\max|\lambda(\sum_{j=1,j\neq i}^{N}(F_{ii}^{-1}F_{ij}))| < 1 \tag{A9}$$

assuming that the first scattered field U_{sca}^{i1} from each fracture is approximately the same. For instance, $\max|\lambda(\sum_{j=1,j\neq i}^{N}(F_{ii}^{-1}F_{ij}))|$ is 0.46 in the second example with 4 inclined fractures at $20Hz$ (Fig. 6). The Born series are converged after 5 iterations.

REFERENCES

[1] M. Schoenberg, "Elastic wave behavior across linear slip interfaces", The Journal of the Acoustical Society of America **68**, 1516–1521 (1980).

[2] J. Hudson, E. Liu, and S. Crampin, "Transmission properties of a plane fault", Geophysical Journal International **125**, 559–566 (1996).

[3] E. Liu, J. Hudson, and T. Pointer, "Equivalent medium representation of fractured rock", Journal of Geophysical Research **105**, 2981–3000 (2000).

[4] E. Liu, S. Crampin, and J. Hudson, "Diffraction of seismic waves by cracks with application to hydraulic fracturing", Geophysics **62**, 253–265 (1997).

[5] F. Sánchez-Sesma and U. Iturrarán-Viveros, "Scattering and diffraction of SH waves by a finite crack: an analytical solution", Geophysical Journal International **145**, 749–758 (2001).

[6] R. Coates and M. Schoenberg, "Finite-difference modeling of faults and fractures", Geophysics **60**, 1514–1526 (1995).

[7] O. Krüger, E. Saenger, and S. Shapiro, "Scattering and diffraction by a single crack: an accuracy analysis of the rotated staggered grid", Geophysical Journal International **162**, 25–31 (2005).

[8] J. Groenenboom and J. Falk, "Scattering by hydraulic fractures: Finite-difference modeling and laboratory data", Geophysics **65**, 612–622 (2000).

[9] S. Vlastos, E. Liu, I. Main, and X. Li, "Numerical simulation of wave propagation in media with discrete distributions of fractures: effects of fracture sizes and spatial distributions", Geophysical Journal International **152**, 649–668 (2003).

[10] R. Slawinski and E. Krebes, "Finite-difference modeling of SH-wave propagation in nonwelded contact media", Geophysics **67**, 1656–1663 (2002).

[11] J. Zhang, "Elastic wave modeling in fractured media with an explicit approach", Geophysics **70**, T75–T85 (2005).

[12] J. Zhang and H. Gao, "Elastic wave modelling in 3-D fractured media: an explicit ap-

proach", Geophysical Journal International **177**, 1233–1241 (2009).

[13] S. Nakagawa, K. Nihei, L. Myer, and E. Majer, "Three-dimensional elastic wave scattering by a layer containing vertical periodic fractures", The Journal of the Acoustical Society of America **113**, 3012–3023 (2003).

[14] T. Pointer, E. Liu, and J. Hudson, "Numerical modelling of seismic waves scattered by hydrofractures: application of the indirect boundary element method", Geophysical Journal International **135**, 289–303 (1998).

[15] U. Iturrarán-Viveros, R. Vai, and F. Sánchez-Sesma, "Scattering of elastic waves by a 2-D crack using the Indirect Boundary Element Method (IBEM)", Geophysical Journal International **162**, 927–934 (2005).

[16] U. Iturrarán-Viveros, F. Sánchez-Sesma, and F. Luzón, "Boundary element simulation of scattering of elastic waves by 3-D cracks", Journal of Applied Geophysics **64**, 70–82 (2008).

[17] T. Chen, M. Fehler, X. Fang, X. Shang, and D. Burns, "SH Wave Scattering from Fratures using Boundary Element Method with Linear Slip Boundary Condition", submitted to Geophysical Journal International, (2011).

[18] M. Bouchon and O. Coutant, "Calculation of synthetic seismograms in a laterally varying medium by the boundary element-discrete wavenumber method", Bulletin of the Seismological Society of America **84**, 1869–1881 (1994).

[19] F. Wuttke, P. Dineva, and T. Schanz, "Seismic wave propagation in laterally inhomogeneous geological region via a new hybrid approach", Journal of Sound and Vibration 664–684 (2010).

[20] B. Hustedt, S. Operto, and J. Virieux, "Mixed-grid and staggered-grid finite-difference methods for frequency-domain acoustic wave modelling", Geophysical Journal International **157**, 1269–1296 (2004).

[21] K. Aki and P. Richards, *Quantitative seismology: Theory and methods*, (Freeman, San Francisco, CA, 1980), Chap.2, pp. 28–30.

[22] P. Martin and F. Rizzo, "On boundary integral equations for crack problems", Proceed-

ings of the Royal Society of London. A. Mathematical and Physical Sciences **421**, 341–355 (1989).

[23] S. Operto, J. Virieux, P. Amestoy, J. L'Excellent, L. Giraud, and H. Ali, "3D finite-difference frequency-domain modeling of visco-acoustic wave propagation using a massively parallel direct solver: A feasibility study", Geophysics **72**, SM195–SM211 (2007).

[24] G. Strang, *Computational science and engineering*, (Wellesley-Cambridge Press, Wellesley, MA, 2007), Chap.7, pp. 563–579.

LIST OF FIGURES

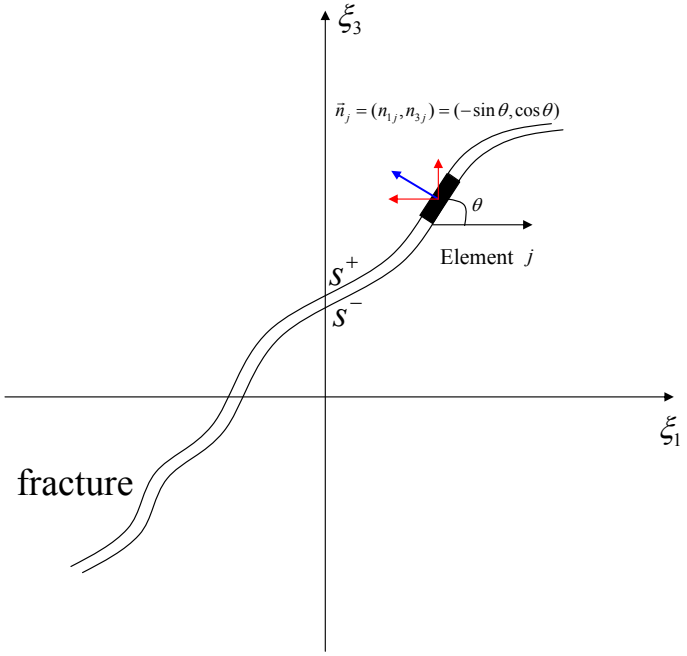
ξ_3
$\vec{n}_j = (n_{1j}, n_{3j}) = (-\sin\theta, \cos\theta)$
θ
Element j
S^+
S^-
ξ_1
fracture

FIG. 1

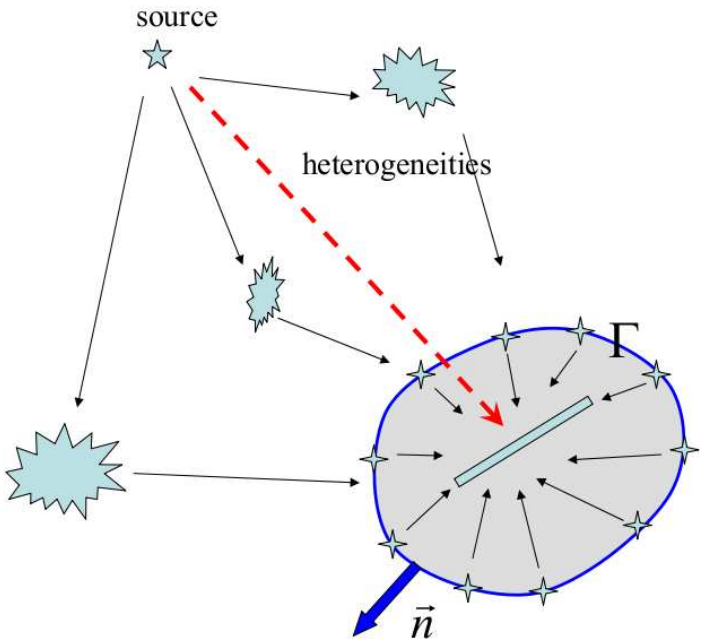

FIG. 2

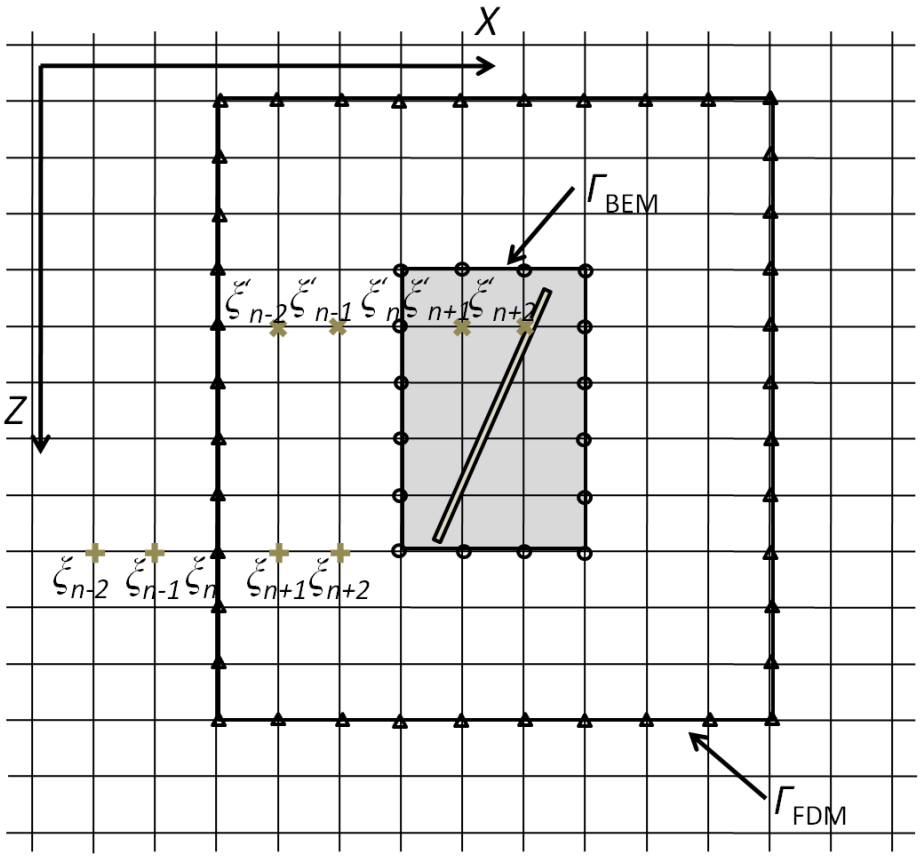

FIG. 3

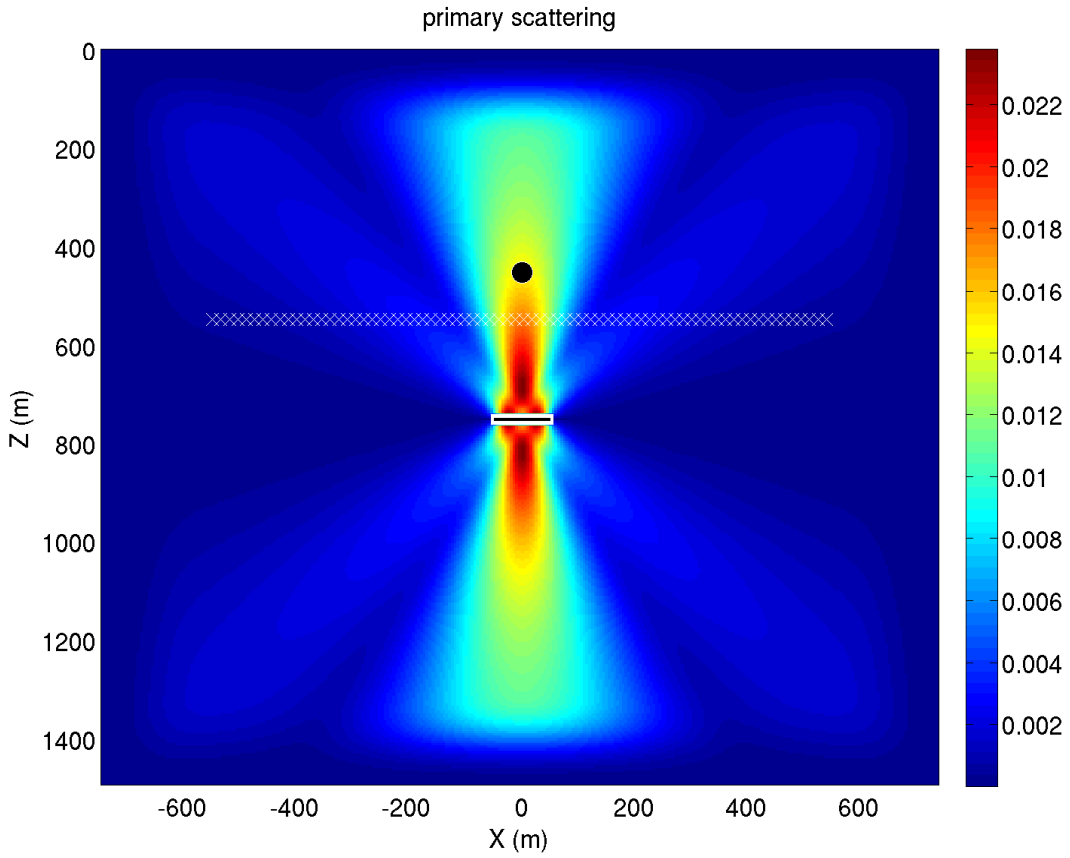
primary scattering
0
200
400
600
800
1000
1200
1400
Z (m)
-600
-400
-200
0
200
400
600
X (m)
0.022
0.02
0.018
0.016
0.014
0.012
0.01
0.008
0.006
0.004
0.002

FIG. 4

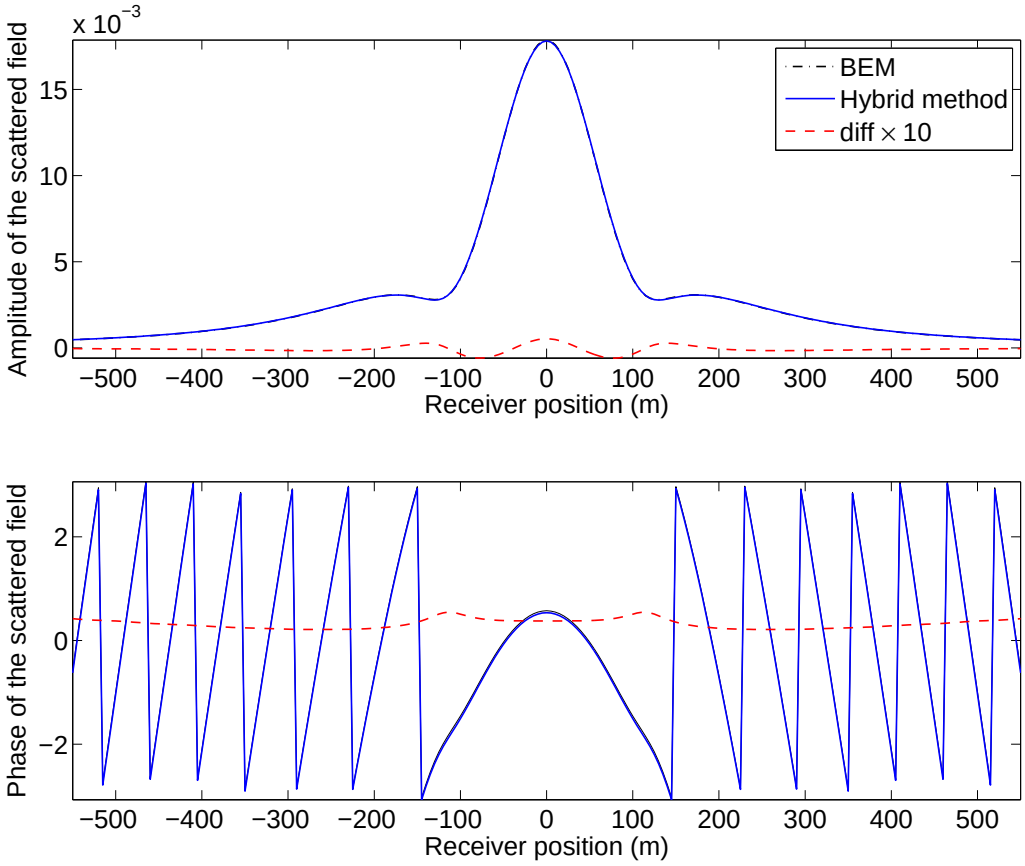
x 10^−3
Amplitude of the scattered field
15
10
5
0
BEM
Hybrid method
diff × 10
−500
−400
−300
−200
−100
0
100
200
300
400
500
Receiver position (m)
Phase of the scattered field
2
0
−2
−500
−400
−300
−200
−100
0
100
200
300
400
500
Receiver position (m)

FIG. 5

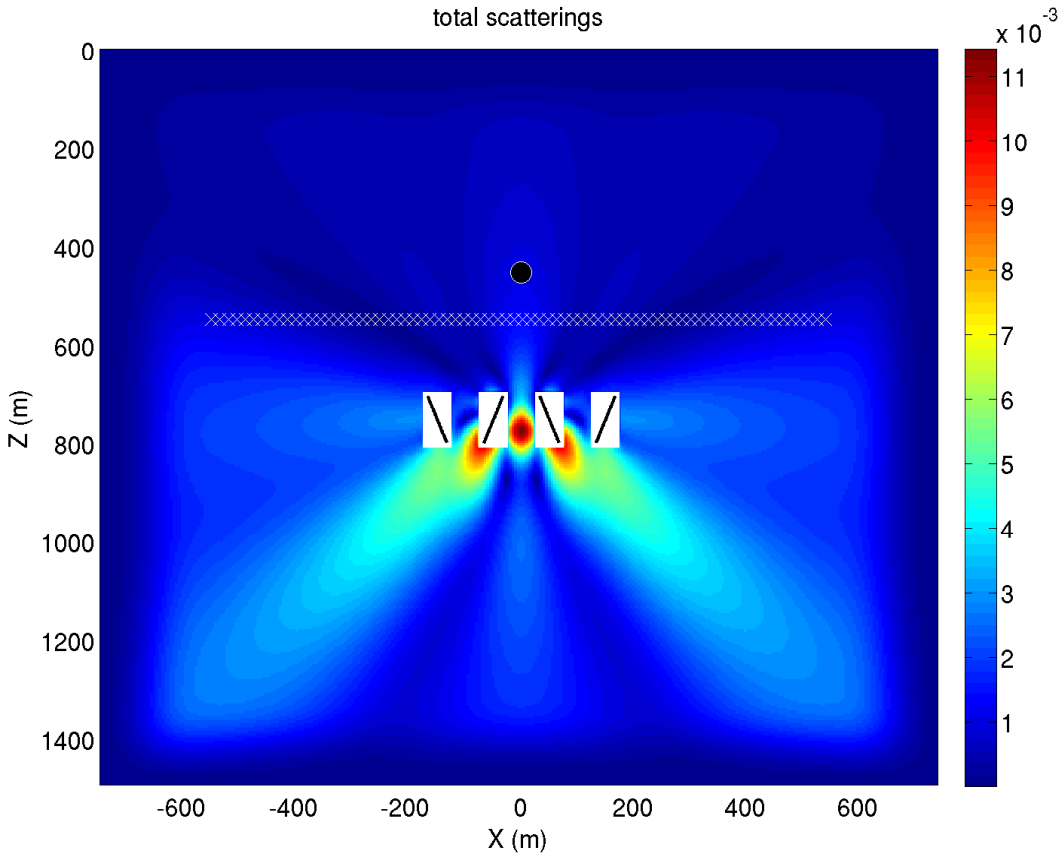
total scatterings
x 10^-3
11
10
9
8
7
6
5
4
3
2
1
0
200
400
600
800
1000
1200
1400
Z (m)
-600
-400
-200
0
200
400
600
X (m)

FIG. 6

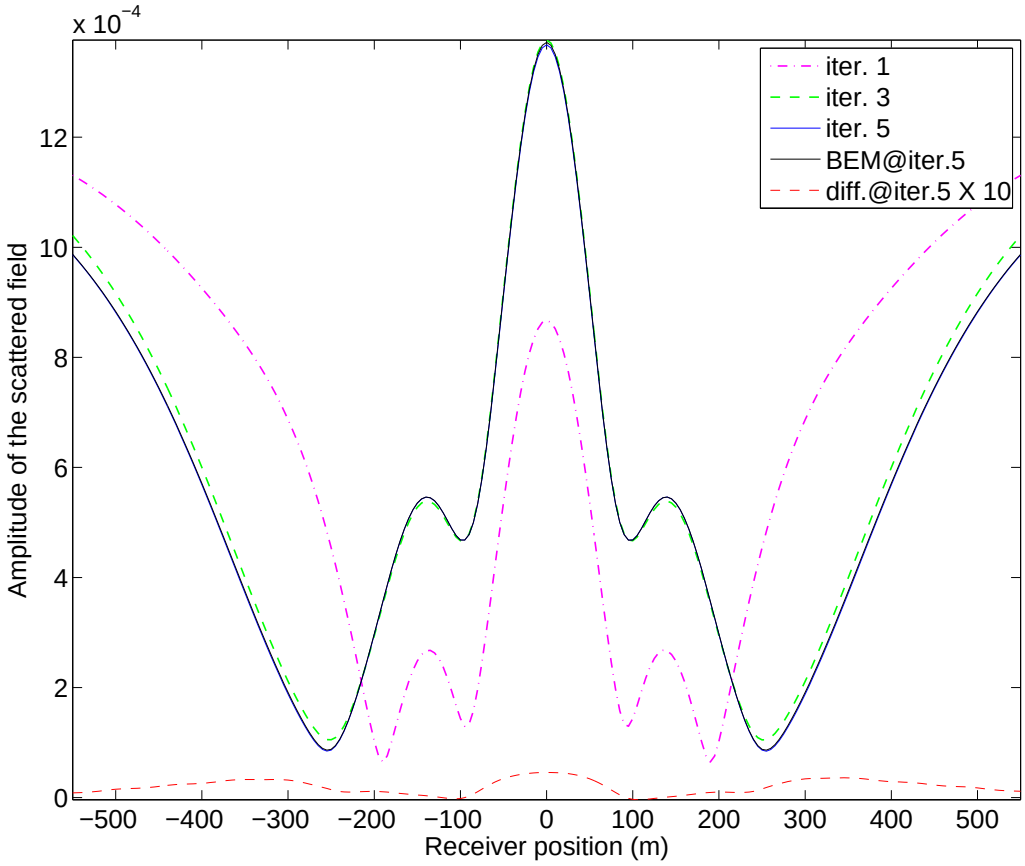
x 10^-4
iter. 1
iter. 3
iter. 5
BEM@iter.5
diff.@iter.5 X 10
Amplitude of the scattered field
Receiver position (m)
0
2
4
6
8
10
12
−500
−400
−300
−200
−100
0
100
200
300
400
500

FIG. 7

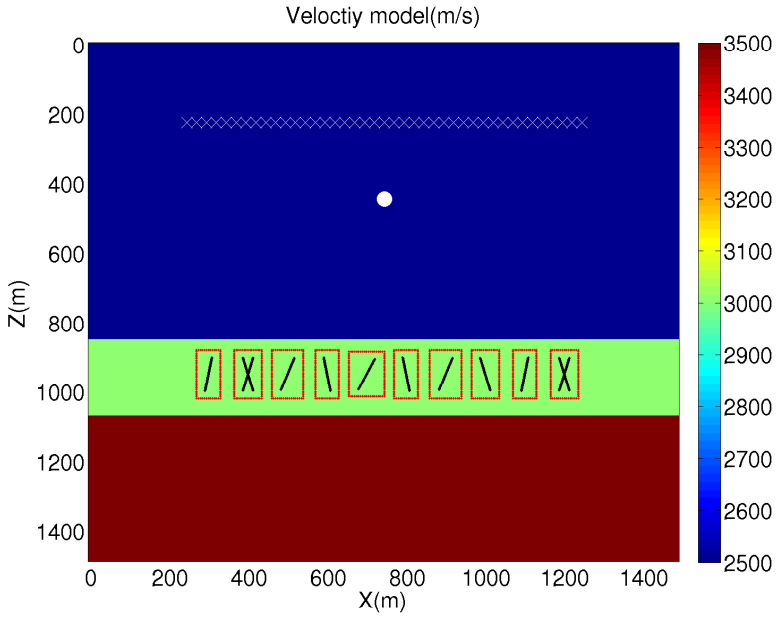
Velocity model(m/s)
Z(m)
X(m)
0
200
400
600
800
1000
1200
1400
3500
3400
3300
3200
3100
3000
2900
2800
2700
2600
2500

FIG. 8

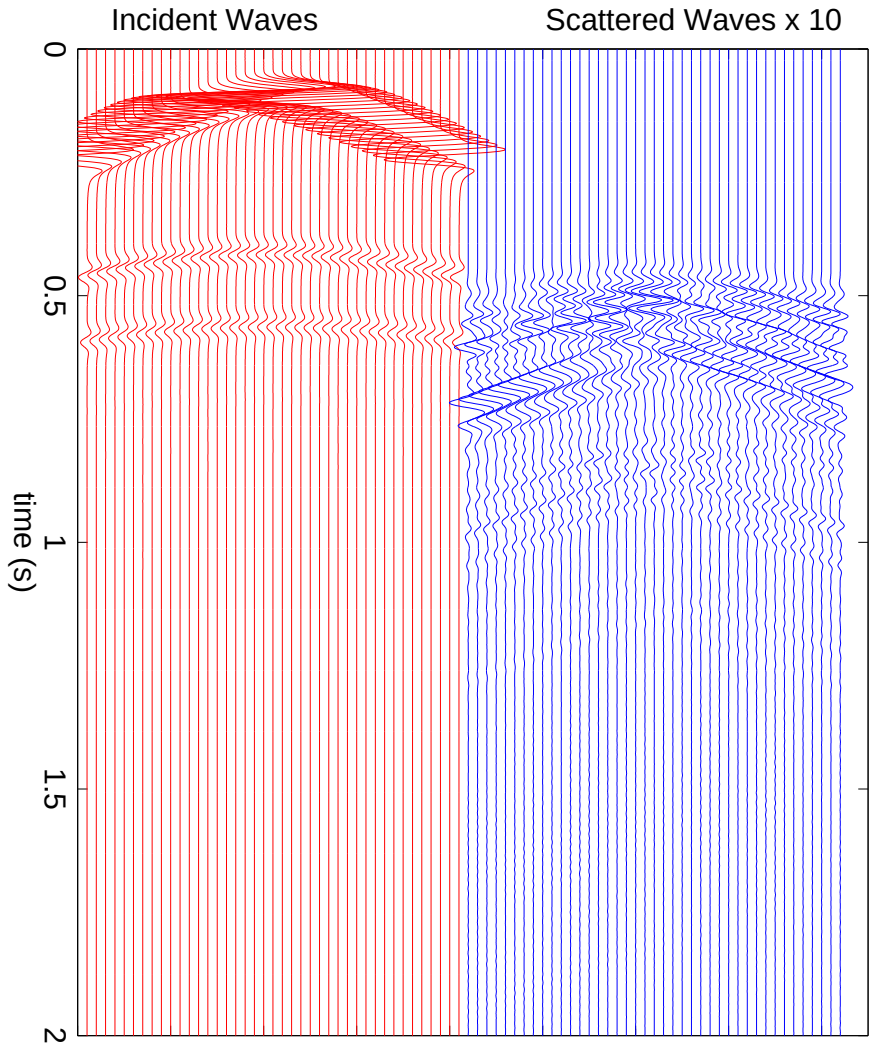

FIG. 9

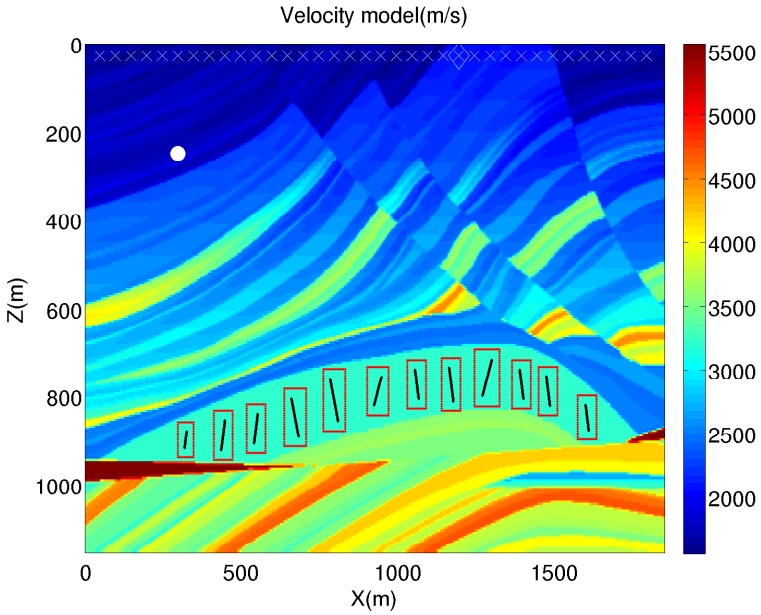
Velocity model(m/s)
0
200
400
600
800
1000
Z(m)
0
500
1000
1500
X(m)
5500
5000
4500
4000
3500
3000
2500
2000

FIG. 10

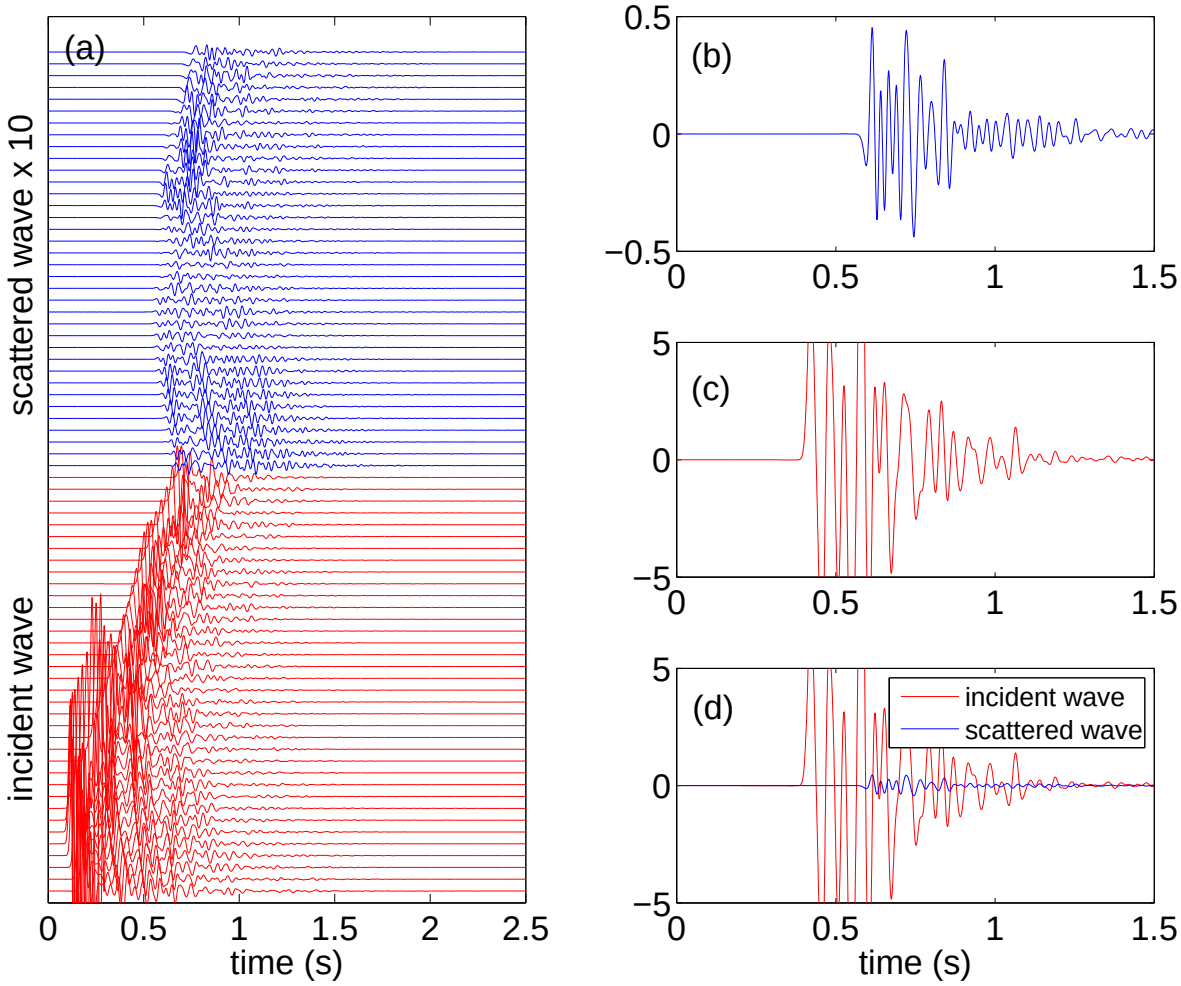
(a)
scattered wave x 10
incident wave
0
0.5
1
1.5
2
2.5
time (s)
(b)
0.5
0
−0.5
(c)
5
0
−5
(d)
incident wave
scattered wave
time (s)

FIG. 11

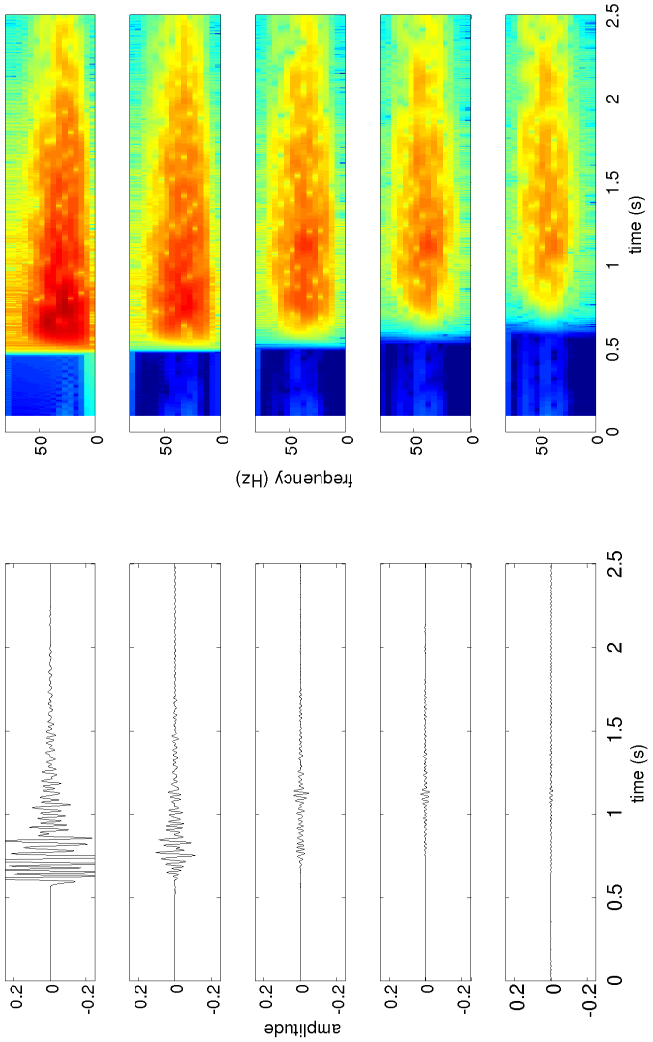

FIG. 12